Chapter 3

A SENSITIVITY ANALYSIS OF ELASTIC DISLOCATION MODELS FOR INTERSEISMIC DEFORMATION IN SUBDUCTION ZONES

3.1 Introduction

At subduction plate boundaries, geodetic data from the interseismic period — decades to centuries after a megathrust earthquake — help to delineate regions of the megathrust that are not presently slipping and can potentially produce large earthquakes. Due to both observational and theoretical considerations, such data are frequently interpreted using simple elastic dislocation models (EDMs). The simplest of these EDMs, the backslip model [the BSM, see Savage, 1983], can be essentially described with only two parameters — the extent of the locked fault interface, and the plate geometry. The BSM has been widely used in modeling interseismic period geodetic data in subduction zones, and to successfully fit geodetic observations using realistic plate interface geometries [Zweck et al., 2002; Khazaradze and Klotz, 2003; Wang et al., 2003; Suwa et al., 2006]. Even when nonlinear rheologies (e.g., elasto-plastic) are assumed for modeling plate deformation, strains tend to localize in narrow zones. The far-field deformation due such shear zones can be hard to distinguish from the field resulting from slip along a single fault, assuming purely elastic rheology [Souter and Hager, 1997]. Also, as the quality of geodetic data improves, they can be used to constrain more complicated 3D models [e.g., Masterlark, 2003].

Owing to the simplicity of EDMs, and their success in fitting current geodetic observations, the analysis presented here is entirely based on such models — specifically, on the BSM. The BSM is motivated by the recognition that the overriding plate apparently experiences little permanent inelastic deformation on the time scales relevant to the seismic cycle (less than a few thousand years) [see, Savage, 1983; Wang and Hu, 2006]. To first order, the interseismic and coseismic strain fields must cancel each other

and asthenospheric relaxation does not significantly contribute to the interseismic deformation field [Savage, 1983, 1995]. In a previous paper [see Chapter 2, and Kanda and Simons, 2010], we showed the equivalence between a subducting plate model (the ESPM) and the BSM, and concluded that owing to practical considerations, the BSM would fit currently available geodetic data as well as the ESPM. For reasons described there, the small effects associated with layering as well as gravity are typically ignored when applying the BSM, a homogeneous elastic half-space is assumed for estimating the firstorder features of the interseismic surface deformation field..

Owing to the rich variety of behavior that can be simulated, as well as their computational speed, such simple EDMs warrant serious consideration when inverting interseismic geodetic data in subduction zones. Even though geometry has a first-order effect on EDM predictions, geometric parameters (and sensitivity to variations in these parameters) are seldom included in slip-inversions because inverting for geometry at the same time as slip distribution can become prohibitively expensive (since Greens functions/kernels have to be re-computed each time fault discretization changes significantly). So, this paper is a purely theoretical effort to systematically analyze, and quantitatively estimate the sensitivity of surface velocity predictions to parameterizations of (i) megathrust interface geometry, and (ii) presence of slip-transition zones along the megathrust interface. By allowing quantitative estimation of uncertainties due to geometrical parameterization, we obtain more accurate constraints on the actual slip deficit along the megathrust interface during the interseismic period.

In the following analysis, the definition of the locked zone during the interseismic period includes both coseismic and postseismic slip zones on the subduction interface. Throughout this paper, we assume Volterra edge-dislocations, i.e., the burger's vector is uniform and constant over the glide-plane of the dislocations — except for the section of the glide surface that is locked ($V_p = 0$) or lies within a slip transition zone (V_p is a linear function) immediately above or below the locked section. We use the 2D elastic dislocation solutions for a dip-slip fault embedded in an elastic half-space given by Freund and Barnett [1976], as corrected by Rani and Singh [1992] (see also, Tomar and

Dhiman [2003] and Cohen [1999]) for computing surface velocities. We quantify the sensitivity of key surface observables — the locations of the hinge-line (x_{hinge}, where the vertical velocities switch from subsidence to uplift during the interseismic, i.e., where $U_z = 0$) and maximum uplift rates in the vertical velocity field (x_{max}, where U_z is a maximum) — to EDM parameters: subduction thrust geometry, the extent of the locked zone, s_{lock}, and the width of a transition zone, s_{trans}, downdip of s_{lock}. We assume that the origin is at the trench, the x-axis is positive "landward" of the trench, and the z-axis is positive upwards (so depths within the half-space are negative). Dips are positive clockwise from the positive x-axis. For the vertical surface deformation field, uplift is considered positive, and for the horizontal field, "landward" motion is assumed positive. If the fault geometry is linear (straight line), a circular arc (constant curvature), or a parabolic profile (decreasing curvature with depth) — all passing through the origin (the trench) — it is straightforward to relate s_{lock} to either D_{lock}, or x_{lock}. Using faults having the same lengths and same dips at the downdip end of the locked zone allows us to compare predictions of surface observables like x_{hinge} and x_{max} for different fault geometries. Although we only consider the 2D problem (the fault is assumed to extend to infinity along strike, in-and-out of the plane of this paper) the analysis here can be easily extended to 3D problems with geometry varying along the strike of the trench axis.

3.2 Transition zones adjoining the locked megathrust

In reality, it is physically implausible for an abrupt transition from locked to creeping at the downdip end of the locked zone, as a dislocation model would imply. Stress concentrations would be too high for the material to behave elastically [e.g., Scholz, 1990]. In addition, the downdip end of the locked zone as well as the surrounding overriding plate is thought to be thermally controlled [Hyndman and Wang, 1993] and experience time-dependent anelastic deformation. So, we make use of a kinematically imposed transition zone along the plate interface downdip of the locked zone as a proxy for the integrated effects of anelastic deformation during the seismic cycle [e.g., Wang et al., 2003]. The width of this transition zone is thought to be controlled by the 350° and

450° isotherms [Hyndman and Wang, 1993], and its location along the subduction interface strongly depends both on the interface geometry as well as the thermal structure for the subduction zone. For instance, Wang et al. [2003] assume a transition zone whose width is as large as the locked zone, governed by different tapered slip distribution profiles at different times during the seismic cycle. Here, in our intuition building toy models, we consider a transition zone whose width is 25% of that of the locked zone (f_{tz}=0.25), along which slip increases linearly from zero to the long-term plate convergence rate during the interseismic period. Such a tapered slip zone is only partially slipping (creeping) during the interseismic period, but also partially ruptures coseismically. Although f_{tz} was arbitrarily chosen here, our purpose is to demonstrate its significant effect of tapered slip zones on the predictions of elastic dislocation models – even when they have such a small extent. For a subducting plate having a finite thickness, as represented in the ESPM, the steady motion of its bottom surface can result in interseismic slip — at velocities less than or equal to the plate convergence rate — along the shallow portion of the plate interface (between the trench and depths of 5–10 km). Such shallow slip is plausible in view of the fact that the frontal wedge of the overriding plate is made up of unconsolidated sediments that do not have significant internal strength. However, slip along the shallow interface must transition from a finite value to zero at the updip limit of the locked zone. As will be shown later, such shallow updip transition zones do not significantly affect the vertical velocities (and hence, surface observables like the locations of the hinge-line and maximum vertical velocity), but strongly affect horizontal velocities within a few locking depths of the trench (~ by as much as 100% of the plate convergence rate). In this study, we use an updip transition zone extending from the trench (where, slip velocity is assigned the plate rate) to the updip limit of the locked zone (where slip is zero during the interseismic), to illustrate the effects of varying its extent. Here, we consider a lower transition zone having a width, s_{trans}, along the plate interface downdip of the locked zone, as well as a shallow transition zone of width $\leq s_{trans}$ along the plate interface between the trench and the updip limit of the locked zone.

We explore the effect of fractional transition zone widths, f_{tr} (= s_{trans}/s_{lock}) in Figure 3-1 (a) through (d). The effect of adding a downdip transition zone is the same as that of increasing s_{lock}, and slightly reducing the effective uniform convergence velocity (averaged over both the fully and partially locked interface) for the interseismic period (Figure 3-1 (a) and (b)). In other words, the velocity profiles from dislocation models having a transition zone are of a longer wavelength (or broader) than those for the case having no transition zone. Also, a transition zone of the same length affects the surface velocity predictions for both the ESPM and the BSM (having the same geometry and convergence velocity), by roughly the same fractional amount. Because the locations of the change in slope of the horizontal velocity profiles follow the effective x_{lock}, it occurs farther than that for the no-transition-zone case. Furthermore, the horizontal velocity profile is broader beyond this change in slope when there is a transition zone. To facilitate comparison, the geometry considered in Figure 3-1 is identical to that considered for the Cascadia subduction zone by Williams and McCaffrey [2001]. The broadening of horizontal velocity profiles due to a downdip transition zone (Figure 3-1 a and b – for the ESPM or the BSM) can help explain the discrepancy between their EDM-predicted and observed horizontal GPS velocities [Figure 3a, Williams and McCaffrey, 2001]. Again, the shapes of the vertical velocity profiles are much more sensitive to the extent of the transition zone (Figure 3-1 (a) and (b) middle), compared to those of the horizontal velocity profiles (Figure 3-1 (a) and (b) bottom).

On the other hand, the vertical surface velocity profiles predicted by either the ESPM or the BSM are not significantly affected by the presence of an updip transition zone (Figure 3-1 (c) and (d)), owing to the typically shallow dip of the plate interface near the trench (which is typical of most subduction interfaces). An updip transition zone causes a large gradient in horizontal surface velocities near the trench, without significantly affecting these velocities landward of x_{lock}. As before, the shapes of the horizontal surface velocity predictions of the ESPM and the BSM are nearly identical, making it hard to use this

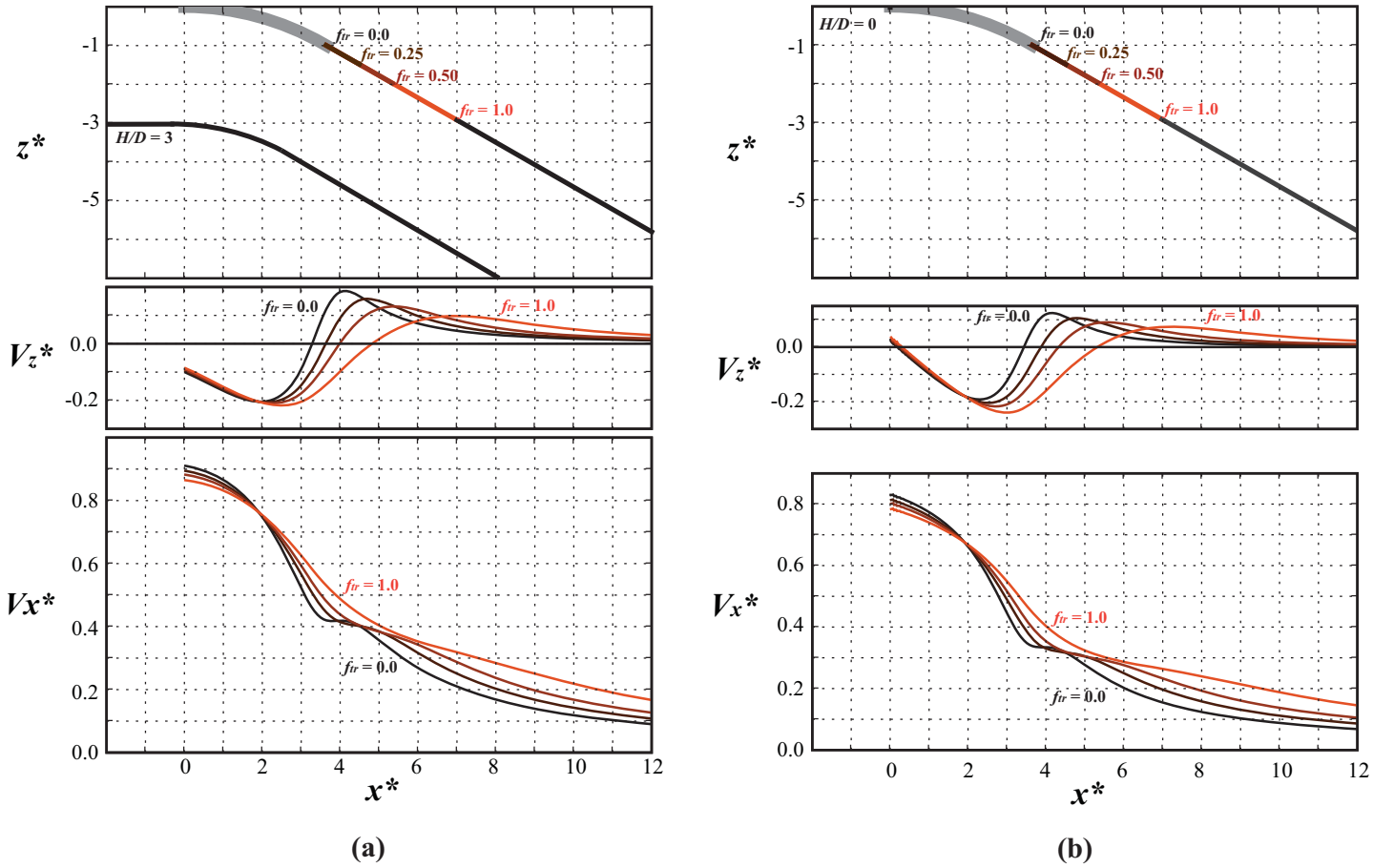
z*
H/D = 3
fir = 0.0
fir = 0.25
fir = 0.50
fir = 1.0
-1
-3
-5
Vz*
0.0
-0.2
Vx*
0.8
0.6
0.4
0.2
0.0
0
2
4
6
8
10
12
x*
(a)
H/D = 0
(b)

Figure 3-1.

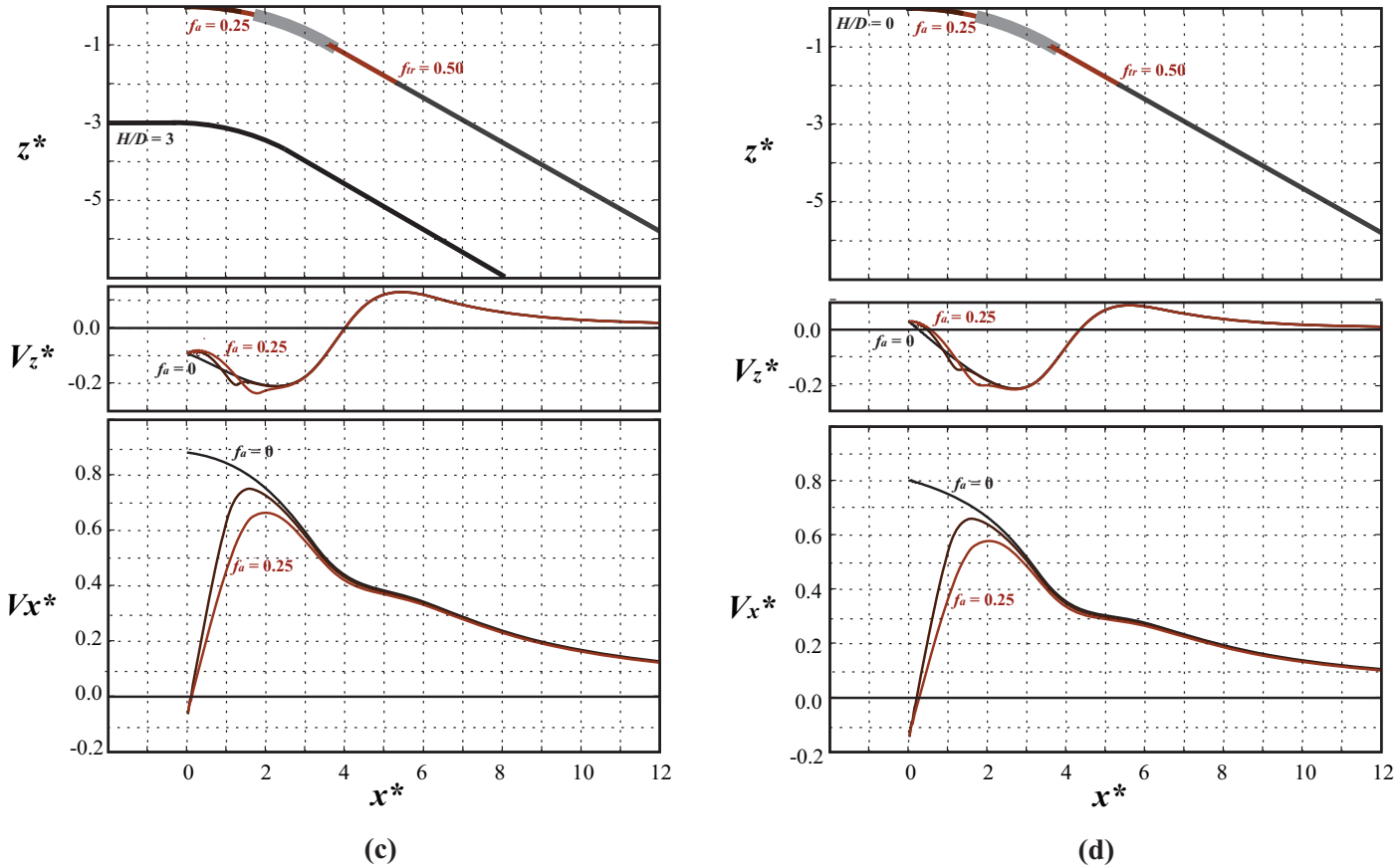

Figure 3-1. Effect of doubling the width of the transition zones updip and downdip of the locked megathrust interface for the ESPM and the BSM. f_{tr} is the fractional length of the transition zone relative to the width of the locked megathrust, s_{trans}/s_{lock}. For updip transition zones (parts a and b), results are presented for f_{tr} = 0, 0.125, and 0.25. For downdip transition zones (parts c and d), results are presented for f_{tr} = 0, 0.25, 0.5, and 1. Axes are as described in text.

component to distinguish between the two models. The vertical surface velocity profiles can still discriminate between the two models, owing to the strong dependence of their shape on both the plate thickness as well as the extent of the downdip transition zone (Figure 3-1 (c) and (d)). Therefore, vertical surface velocities are the key to not only differentiating between the ESPM and the BSM (i.e., for estimating the minimum elastic plate thickness for a given subduction interface geometry), but also the location of the effective x_{lock}. However, the uncertainties in horizontal velocities are smaller than those for the verticals (sometimes by a factor of two), and for most subduction zones or thrust faults (which typically have dips < 30° near their surface trace), surface horizontal velocities are much larger than the verticals, and therefore have a much better signal-to-noise ratio compared to the verticals. The relative importance of horizontal and vertical velocity data in inverting geodetic data is investigated next, using an idealized distribution of noisy, "synthetic" observations derived from the ESPM having different plate thicknesses.

3.3 Inverting geodetic data using the ESPM vs. the BSM

We performed a general Monte Carlo simulation to determine the potential error incurred in inverting geodetic data using the BSM as opposed to the ESPM. We generate synthetic data (horizontal and vertical surface velocities) assuming that subduction zones in the real Earth are represented by ESPMs having different plate thicknesses. The ESPM is characterized by three independent parameters of practical interest — fault dip, θ, length of the locked megathrust (extending downdip from the trench along the plate interface), s_{lock}, and the plate thickness, H (H/D_{lock} = 0.01 (nearly identical to the BSM), 1, and 3 are presented in the respective columns of Figure 3-2 (a), (b) and (c)). For simplicity, we use a planar megathrust interface geometry having a dip, θ = 25°, and depth of locking, D_{lock} = 40 km, corresponding to a fault width, s_{lock}, of ~ 95 km). Our principal conclusions here would not differ qualitatively for curved plate geometry. Although typical geodetic inversions do not invert for geometry, we include the sensitivity of the misfits to variations in dip, in order to emphasize the importance of

tightly constraining this parameter at the outset. We show that the minimum BSM misfits become biased — that is, the best fit BSM would predict a wider fault with a shallower dip — with increasing subducting plate thickness. If dip were tightly constrained (using seismic data, for instance), then the extant of the locked zone along the megathrust can be better constrained. The generalized Monte Carlo approach used here consists of the following steps:

a) We assume a Gaussian distribution for noise, having zero means and standard-deviations of $0.02V_p$ for the horizontals and $0.03\ V_p$ for the verticals — or 2 and 3 mm/yr, respectively, if V_p = 10 cm/yr.
b) Next, one thousand samples of the noise in vertical and horizontal data are generated from the above distributions for the ESPM having a given H (perturbations: δV_x, δV_z). These perturbations are then added to the respective ESPM surface velocity fields (synthetics: V_x, V_z) to generate "noisy" datasets ($V_x + \delta V_x$, $V_z + \delta V_z$).
c) Finally, the BSM with the smallest misfit to each noisy (synthetic) dataset — consisting of only the vertical velocities, only the horizontal velocities, or verticals-plus-horizontals (presented in respective rows of a, b and c) — is estimated via a grid-search in the θ - s_{lock} parameter space for a given H.

The closest geodetic observation on the overriding plate was assumed to be 100 km landward from the trench — a typical distance for most subduction zones — and observations were assumed to be uniformly spaced at 5 km intervals. Increasing observation station spacing, or using a different set of ESPM parameters for generating the synthetic surface velocity data would not qualitatively change our conclusions. With such uniform and dense spacing, we are assuming that we have a high-resolution dataset (e.g., GPS and InSAR imagery) to understand the model-based limitations of the inversion process, given the "best-case scenario" data. Here, we use the arc-length of the locked zone, s_{lock}, for parameterization. Had we chosen either D_{lock} (= $s_{lock}\, sin(\theta)$) or x_{lock} (= $s_{lock}\, cos(\theta)$) instead, we would have observed positive and negative correlations (respectively) between these parameters and fault dip, since the steeper the best-fit BSM fault, the deeper its D_{lock}, and smaller its x_{lock}. By using s_{lock}, we avoid these obvious

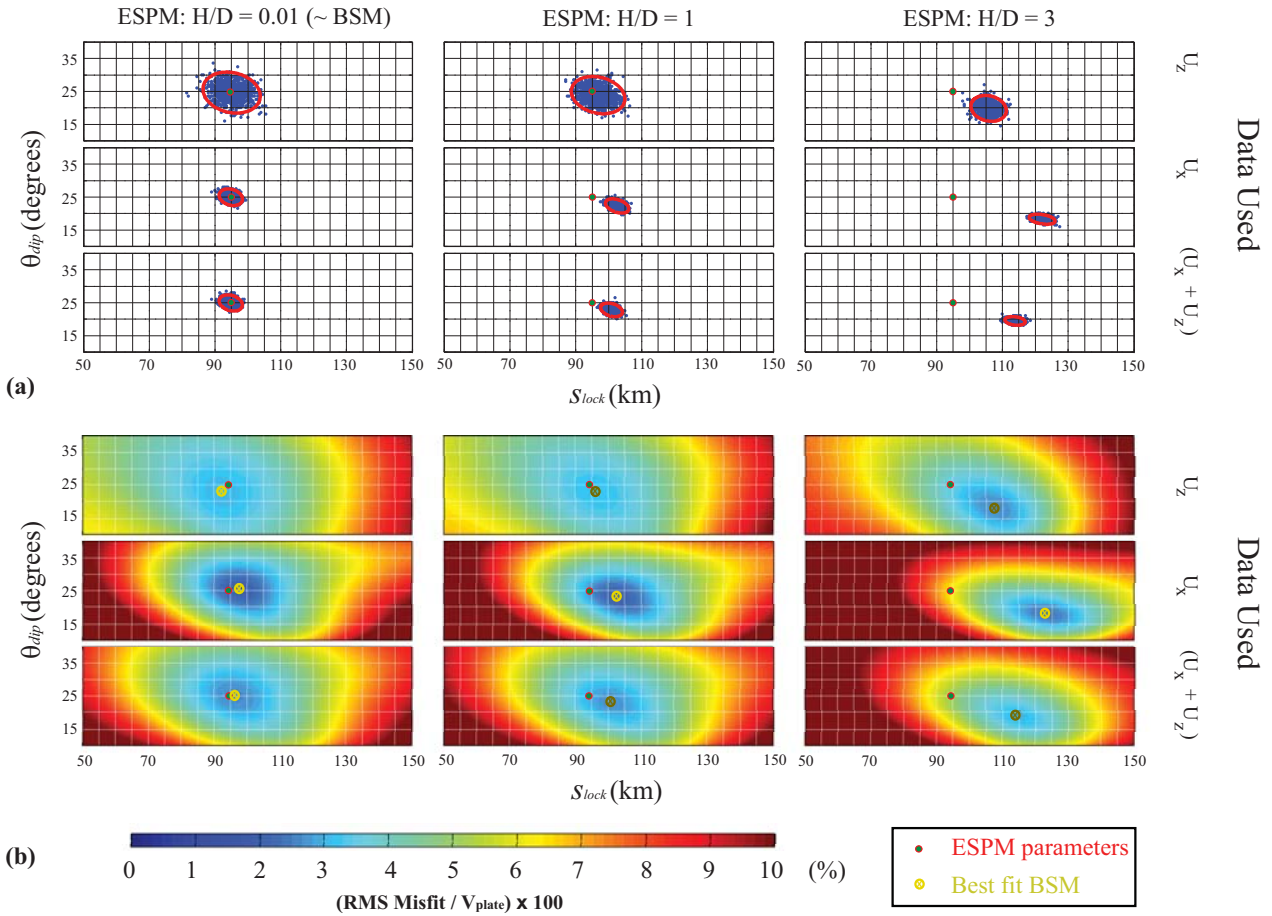
ESPM: H/D = 0.01 (~ BSM)
ESPM: H/D = 1
ESPM: H/D = 3
(a)
(b)
θdip (degrees)
Slock (km)
Data Used
uz
ux
(ux + uz)
0 1 2 3 4 5 6 7 8 9 10 (%)
(RMS Misfit / Vplate) x 100
ESPM parameters
Best fit BSM

Figure 3-2.

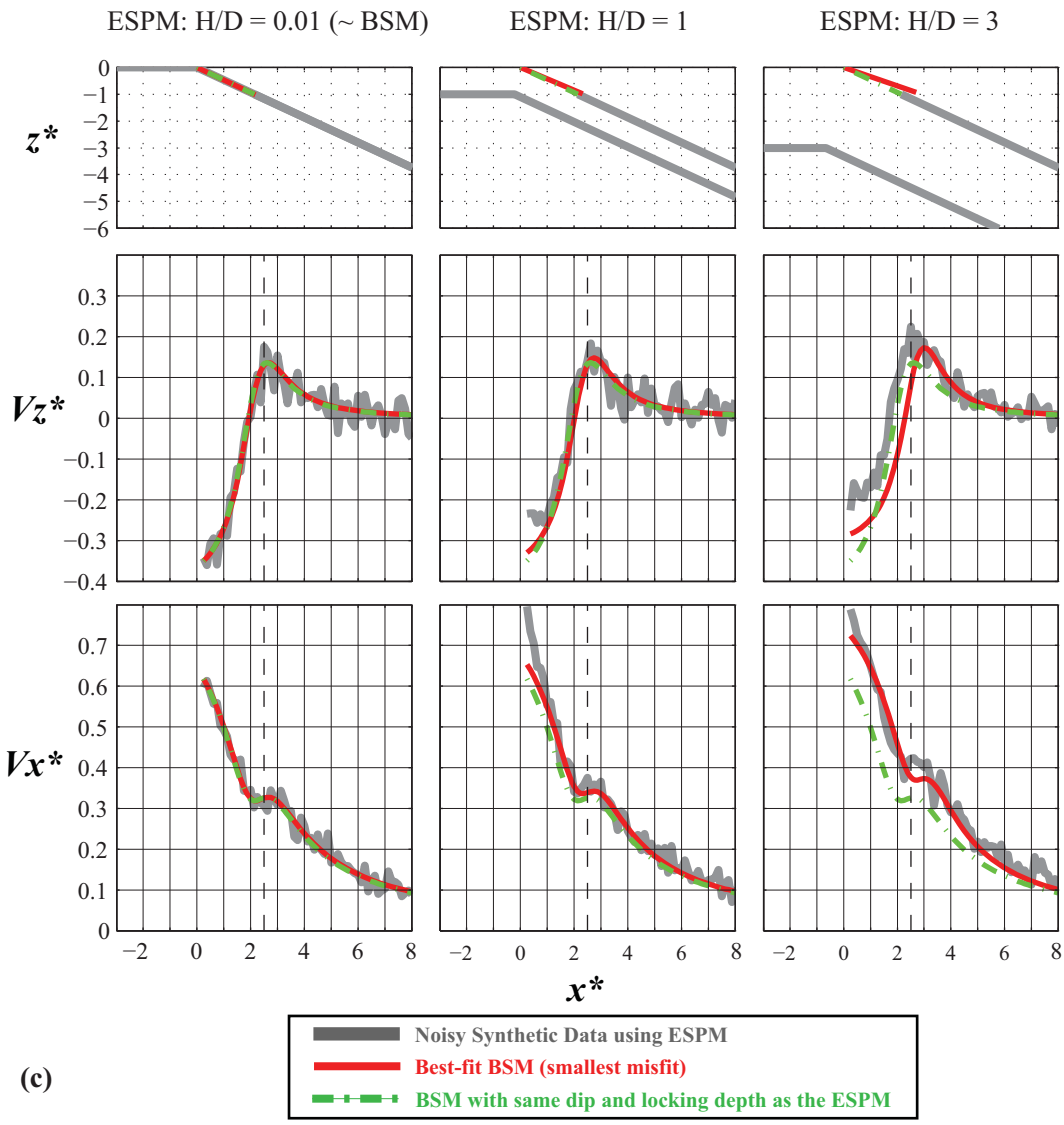

Figure 3-2. BSM inversions of ESPM synthetics. Each column represents results for a given plate-thickness to locking depth ratio: H/D_{lock} = 0.01 (BSM), 1, and 3. (a) 1000 best-fit BSM in the s_{lock}-θ parameter space that fit as many samples of ESPM-based noisy synthetic data for the specified H/D_{lock} ratio. Shown are the lowest misfit solutions satisfying only vertical data (top row), only horizontal data (middle row), and sum of the two datasets (bottom row). The corresponding 1-σ error-ellipses are shown in red. (b) Misfit between the BSM at each point in the s_{lock} -θ parameter space and one of the synthetic data samples in (a). (c) Best-fit backslip model (solid red line), satisfying both the horizontal and vertical synthetic data (solid gray lines) — corresponding to the yellow ⊗ in the bottom row of (b). The best-fit BSMs are as follows: θ = 25°, D_{lock} = 40 km (identical to the ESPM, for column 1); θ = 22.5°, D_{lock} = 38.3 km (column 2); and θ = 20°, D_{lock} = 39.3 km (column 3). The BSM corresponding to θ = 25°, and D = 40 km (dashed green line) is also shown. The top row shows the subduction zone geometry, the middle row shows vertical velocities, and the bottom row shows horizontal velocities. Dashed vertical lines mark the nearest geodetic observation point to the trench

.

correlations. The best fitting BSM was found by computing the L_2-norm of the misfit at every point of the discretized s_{lock}-θ parameter space — having limits of 0-200 km, and 0-45°, respectively — and discretized at a resolution of 0.5 km x 0.5° for each H/D_{lock} ratio.

Owing to their larger signal-to-noise ratio, the best-fit BSM for the combined (horizontal-plus-vertical) datasets are controlled by the errors in horizontal velocities (note the similarity of the misfit surface for the bottom two rows in Figure 3-2(a)). In the limit of small plate thickness, the geometry of the best-fit BSM corresponds to that of the thin plate ESPM, and the centroids of the error ellipses (which give the most likely model parameter estimates) are nearly the same as the original parameters used to generate the ESPM synthetic data, irrespective of the velocity component(s) considered. This similarity implies that given a dense dataset with randomly distributed data errors, if we repeatedly sample a subset of the data for inverting a BSM, after a sufficient number of samples, we will be able to obtain the "true" model parameters. However, a given sample in this distribution of models can be off by as much as 10% in estimating the extent of the locked zone, s_{lock}, which translates into ~ 5% error in estimating the locking depth, d_{lock}, for typical dips found in subduction zones. Furthermore, as the plate thickness increases, and stresses are released episodically in the shallow portions of the subduction zone, the best-fit models collapse into an error-ellipse having much smaller dimensions and a biased centroid, indicating that the region of small misfits both shifts and shrinks as H increases.

We would expect the minimum misfit region of the parameter space to shrink because the synthetic data (from the ESPM) have a variability (plate thickness, H) that the forward model (the BSM) cannot capture and therefore, the overall misfits would become larger, shrinking the regions of low misfit in the parameter space. The minimum misfit region would shift because the effect of increasing H is larger for larger s_{lock} and θ. By taking the L_2-norm misfit surface as well as the minimum misfit model for one of the data-sets randomly chosen from each panel of Figure 3-2(a), we obtain Figure 3-2(b) – in which this shrinking of the low misfit regions can be clearly seen going from the right to the left columns. If a different data-set were chosen, the misfit surface would look slightly different with a different best fit model, but clearly, the error ellipses (Figure 3-2(a))

reside in the corresponding minimum misfit troughs, which also shrink in size with increasing plate thickness (Figure 3-2(b)). If the dip of the fault-segment undergoing rupture is tightly constrained from teleseismic studies, then the minimum misfit lies along a horizontal line corresponding to that dip (25° in this case), thus constraining s_{lock} (and hence, x_{lock} and D_{lock}) more tightly.

Therefore, if the BSM is used to fit interseismic geodetic data, the mean of the best-fit models (the centroids of the ellipses in Figure 3-2(a)) always underestimates θ or overestimates s_{lock}, if plate thickness is non-negligible — that is, the BSM typically predicts a wider-deeper fault, if dip were well constrained. The overestimation of locking depth stems from the main effect of plate thickness on the ESPM predicted surface velocities — above the locked zone, both the horizontal and vertical velocity profiles landward of x_{hinge} are higher (as well as broader) than those for the corresponding BSM. The BSM with a wider fault (or shallower dip) has exactly the same amplification effect above the locked zone (Figure 3-2(c), which presents the best fit models for inversions based on the vertical-plus-horizontal data-set). When the observing stations are located sufficiently far from the trench, as is frequently the case, the error associated with the underestimation of θ or overestimation of s_{lock} is small, and the BSM does a good job of fitting the observations.

3.4 Sensitivity of surface observables to parameterizing the BSM and the ESPM

In view of the wide applicability of the BSM, it is important to understand the sensitivity of surface observables to parameterization of the BSM, especially interface geometry. It has long been known that the geometry of the plate interface has a first-order effect on the surface velocity predictions of dislocation models.

Figure 3-3 presents the effect of fault curvature on the BSM surface velocity predictions. The geometry presented in the figure is similar to that inferred for the Sumatran

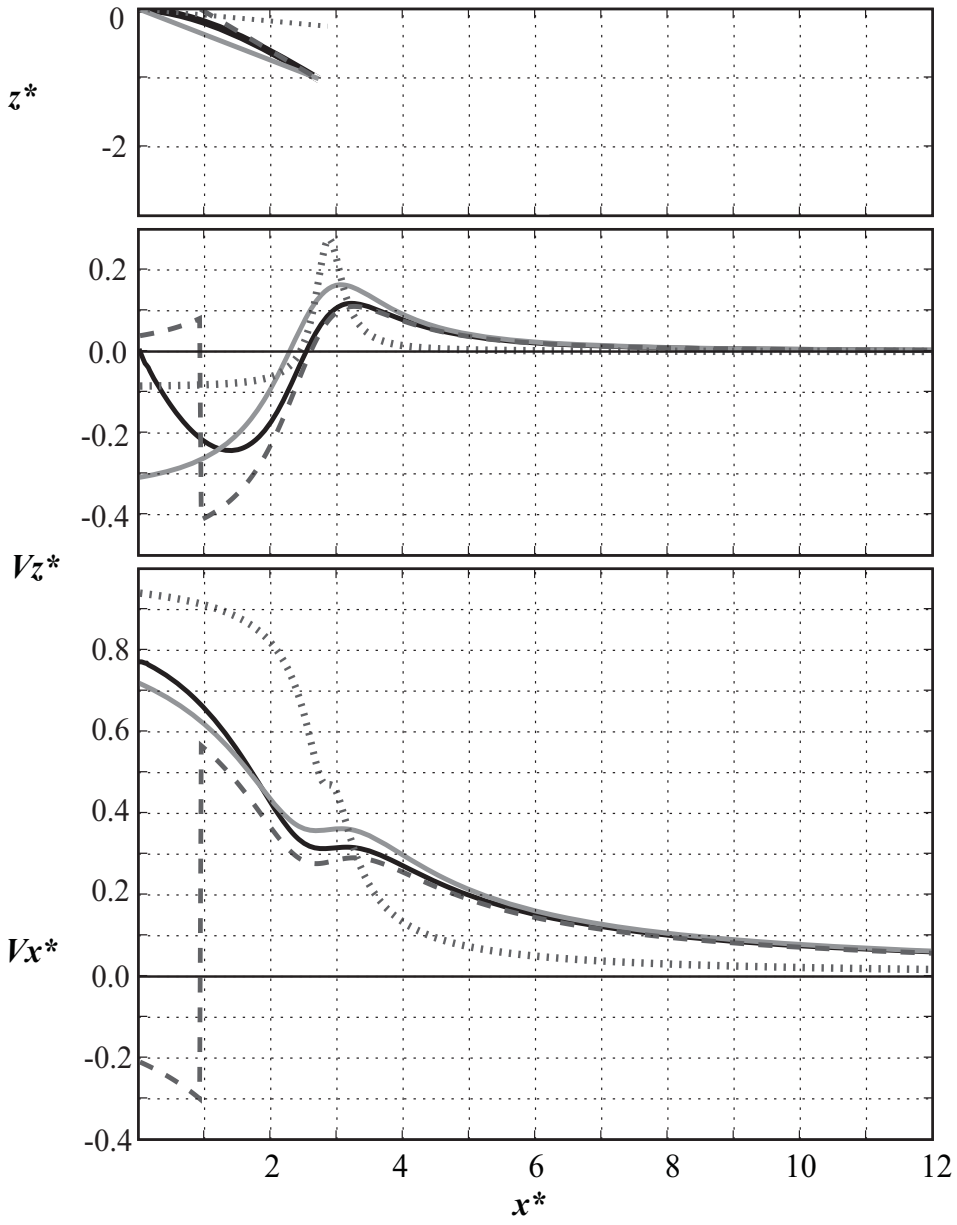

Figure 3-3. Effect of curvature on the BSM surface velocity predictions. The curved fault (solid black line) resembles the subduction thrust interface geometry below the island of Nias, offshore of Sumatra (θ_{top} = 3°, θ_{bot} = 27° [Hsu et al., 2006]). The gray solid line represents a planar fault having the same end-points as the curved fault, and the dashed gray line represents the tangent-approximation to the curved fault. The dotted line represents a shallow dipping fault that approximates the shallow part of the curved interface. See text for details. The top row presents the fault in cross-sectional view. In all cases, uniform normal slip was imposed on the fault patch. Plot axes are as described in text.

subduction zone in the area of the 28 March 2005, (M_w 8.7) Nias-Simeulue rupture [Engdahl et al., 2007]. The effect of curvature is to stretch the velocity profiles non-linearly near either end. Compared to the velocity field of the planar fault having the same end-points, the curved fault behaves like a shallower dipping planar fault with a smaller locking depth near the trench; the curved geometry predicts a shorter-wavelength velocity profile, with a smaller subsidence (Figure 3-3 middle) but larger horizontal compression (Figure 3-3 bottom) near the trench. But away from the trench, the curved fault velocity profiles resemble the broader fields characteristic of a planar fault having a steeper dip (lower peak amplitude of vertical and horizontal velocities above the bottom of the locked patch). Also, above the bottom of the locked zone (and farther landward), the curved fault velocities are nearly identical to those of a steeper but shorter planar fault extending tangentially to the surface (dashed gray line).

Given that geodetic data in subduction zones are typically available starting at distances comparable to x_{lock} from the trench, and the surface velocity profiles at these distances for a curved fault and its downdip tangential approximation are nearly indistinguishable, it may be reasonable to use this tangential fault approximation for modeling far-field landward surface velocities [Chlieh *et al.*, 2004; Simoes *et al.*, 2004; Chlieh *et al.*, 2008b]. However, the tangential fault intersects the free surface landward of the trench, while the location and slope of the tangent fault is highly sensitive to the width of the locked zone, s_{lock}. Also, in this case, interseismic deformation is modeled to be due to slip on the tangent fault, while coseismic deformation is due to slip on the curved (or any non-planar) fault — which is kinematically inconsistent. Therefore, as Savage [1983] originally asserted, if the geometry of the seismogenic zone of the megathrust is known to be curved, then this surface should be used for the BSM as well. Figure 3-3, therefore, demonstrates the significant effect of fault geometry on interpreting geodetic data where data above the locked patch and/or in the vicinity of the trench may become available in the near future.

We next consider the sensitivity of surface observables x_{hinge} and x_{max} to the BSM parameterization — specifically, we explore the values for these observables relative to x_{lock} (Figure 3-4). Although x_{lock} can be directly inverted from geodetic data (especially

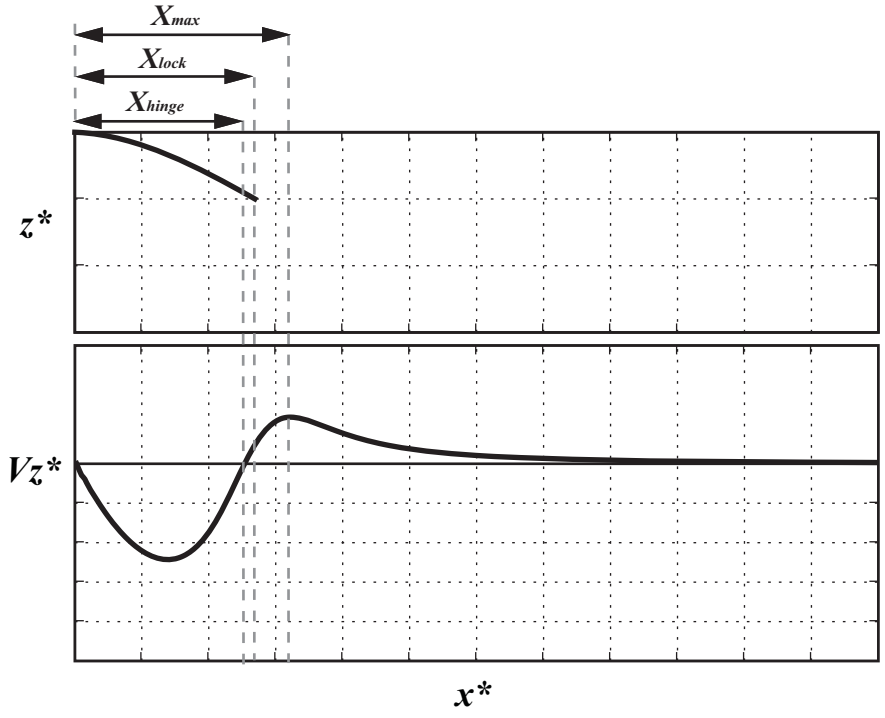

Figure 3-4. Schematic illustration of the relative locations of surface observables, x_{hinge}, x_{lock}, and x_{max}, using the vertical velocity profile for the curved fault presented in Figure 3-6.

from the vertical velocity field), being able to constrain that parameter using x_{hinge} or x_{max} (or both) — in addition to constraining dip from teleseismic observations — can allow us to better constrain the remaining BSM parameter, f_{tr} (= s_{trans}/s_{lock}). So, here we quantify how the dimensionless distances between x_{lock}, and x_{hinge}, x_{max}, their mean, or their difference, vary with fault dip, θ for generalized fault geometries. By normalizing these distances with x_{lock} , our results can be made independent of s_{lock}. We start with the analytical expression for the surface vertical velocity due to an edge-dislocation in a half-space, normalized by the geologic plate convergence rate, V_p, v_y^*, as a function of trench perpendicular distance, x, dip, θ, and fault width, s (corrected version of Freund and Barnett [1976] — see Savage [1983], and Rani and Singh [1992]):

$$v_y^* = \frac{v_y}{V_p} = \frac{\sin(\theta)}{\pi}\left[\left(\frac{xs.\sin(\theta)}{x^2+s^2+2xs.\cos(\theta)}\right)+\tan^{-1}\left(\frac{x-s\cos(\theta)}{s.\sin(\theta)}\right)-\frac{\pi}{2}\right]. \quad (1)$$

To find the hinge-line location, x_{hinge}, we set the above equation to zero, and solve the resulting transcendental equation numerically using a non-linear root-finding algorithm. Although not obvious from the above equation, for nearly vertical faults (as θ tends to 90°), x_{hinge} tends to infinity, and as θ tends to 0°, x_{hinge} tends to a value close to (but less than) s. As Savage [1983] has already shown, the location of the maximum velocity, x_{max}, can be obtained by differentiating (1), setting the result to zero, and solving for x. The final result is:

$$x_{\max} = \frac{s}{\cos(\theta)} = s.\sec(\theta) \ . \tag{2}$$

For nearly vertical faults, (as θ tends to 90°), x_{max} tends to infinity (but at a faster rate than x_{hinge}) and as θ tends to 0°, x_{max} tends to s. As discussed previously, the depth of locking, D_{lock}, equals $s.sin(\theta)$; the surface projection of the bottom of locked fault is given by,

$$x_{lock} = s.\cos(\theta). \tag{3}$$

For nearly vertical faults (θ tends to 90°), x_{lock} tends to zero, but at a much slower rate than either x_{max} or x_{hinge} blow up; as θ tends to 0°, x_{lock} tends to s. For the analysis here, we choose as our independent parameters, the locked fault width, s, and fault dip, θ, which naturally fall out of the analytical solution (1). The theoretical solutions shown in the last three equations are plotted as yellow curves, wherever they appear in Figure 3-5 (a) and (b). For curved faults, faults with downdip transition zones, as well as the ESPM, we first compute the vertical surface velocity field (U_z), for every combination of θ and s, at a resolution of 0.5° x 50 km. We then search for the locations of both the hinge-line ($U_z = 0$) and maximum vertical velocity ($U_z' = 0$). To verify our code, we compute these locations for the planar fault case and check that they plot right on top of the theoretical solutions (Figure 3-5(a)).

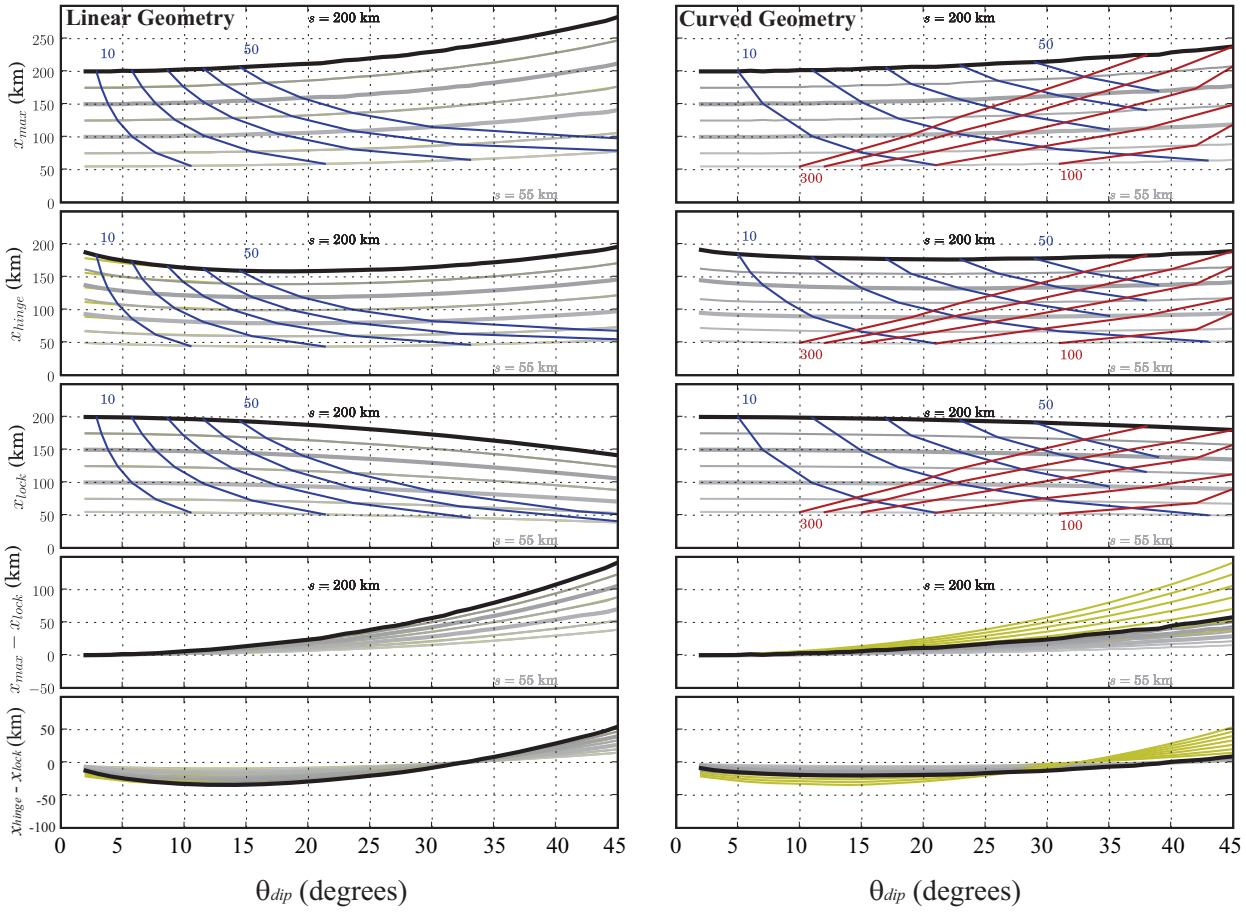

Figure 3-5. Location of the maximum vertical velocity (x_{max}), zero vertical velocity (x_{hinge}), the surface projection of the bottom of locked fault (x_{lock}), and the differences between them, as a function of the length of the locked fault patch, *s*, and dip angle, θ. Each parameter is plotted for *s* ranging from 25 to 200 km, in steps of 25 km. Thicker curves represent fault lengths of 50, 100, 150, and 200 km. (a) Planar faults: Blue curves (cutting across the s-curves from the top left to bottom right) are lines of constant locking depth (10 to 50 km, in steps of 10 km). Theoretical estimates are presented in dark yellow. (b) Curved faults: Red curves (cutting across the s-curves from the bottom right to top left) are lines of constant radii of curvature (100 to 300 km, in steps of 50 km). Blue curves are the same as in (a). Theoretical estimates for planar faults are presented in yellow in the bottom two panels for comparison to (a).

Owing to the simple geometrical parameterizations used to generate linear or curved subduction profiles here, x_{hinge}, x_{max}, and x_{lock} are directly proportional to the fault width, s_{lock}. Therefore, dividing by x_{lock} removes any dependence on fault width, and curves for different s_{lock} collapse into a single curve (Figure 3-6). Figure 3-6 presents the variation of x_{hinge} and x_{max} as a function of θ (for any s_{lock}) for planar faults without a downdip transition zone (Figure 3-6(a)), curved faults without a downdip transition zone (Figure 3-6(b)), planar faults having a downdip transition zone (Figure 3-6(c)), and curved faults having a downdip transition zone (Figure 3-6(d)). Within each part, the first (top) panel presents the dimensionless distance between x_{max} and x_{lock}, relative to x_{lock}:

$$\Delta x_m^* = (x_{max}-x_{lock})/x_{lock} . \quad (4)$$

The second panel presents the dimensionless distance between x_{hinge} and x_{lock}, relative to x_{lock}:

$$\Delta x_h^* = (x_{hinge}-x_{lock})/x_{lock} . \quad (5)$$

The third panel presents the mean of (4) and (5), i.e., the dimensionless mean of x_{hinge} and x_{max}, $\Delta X_M^* = (\Delta x_m^*+\Delta x_h^*)/2$. The fourth panel presents the difference between Equations 4 and 5, i.e., the distance between x_{hinge} and x_{max}, $\Delta X_D^* = (\Delta x_m^*-\Delta x_h^*)$. Finally, the fifth (bottom) panel presents the ratio of x_{hinge} and x_{max} (which is always less than 1.0). Ranges of θ within which x_{hinge}, x_{max}, or some combination of the two is a good predictor for the location of x_{lock} for the BSM are highlighted by gray boxes in Figure 3-6 and encapsulated in Table 3-1 (for faults without a downdip transition zone) and Table 3-2 (for faults with a downdip transition zone, f_{tr} = 25%). As noted previously, updip transition zones do not significantly affect vertical velocities, and therefore, do not influence the values of these surface observables significantly. For the ESPM (not shown), the variation of these dimensionless parameters with dip angle is qualitatively similar to that for the corresponding BSM, but with wider uncertainty relative to x_{lock}.

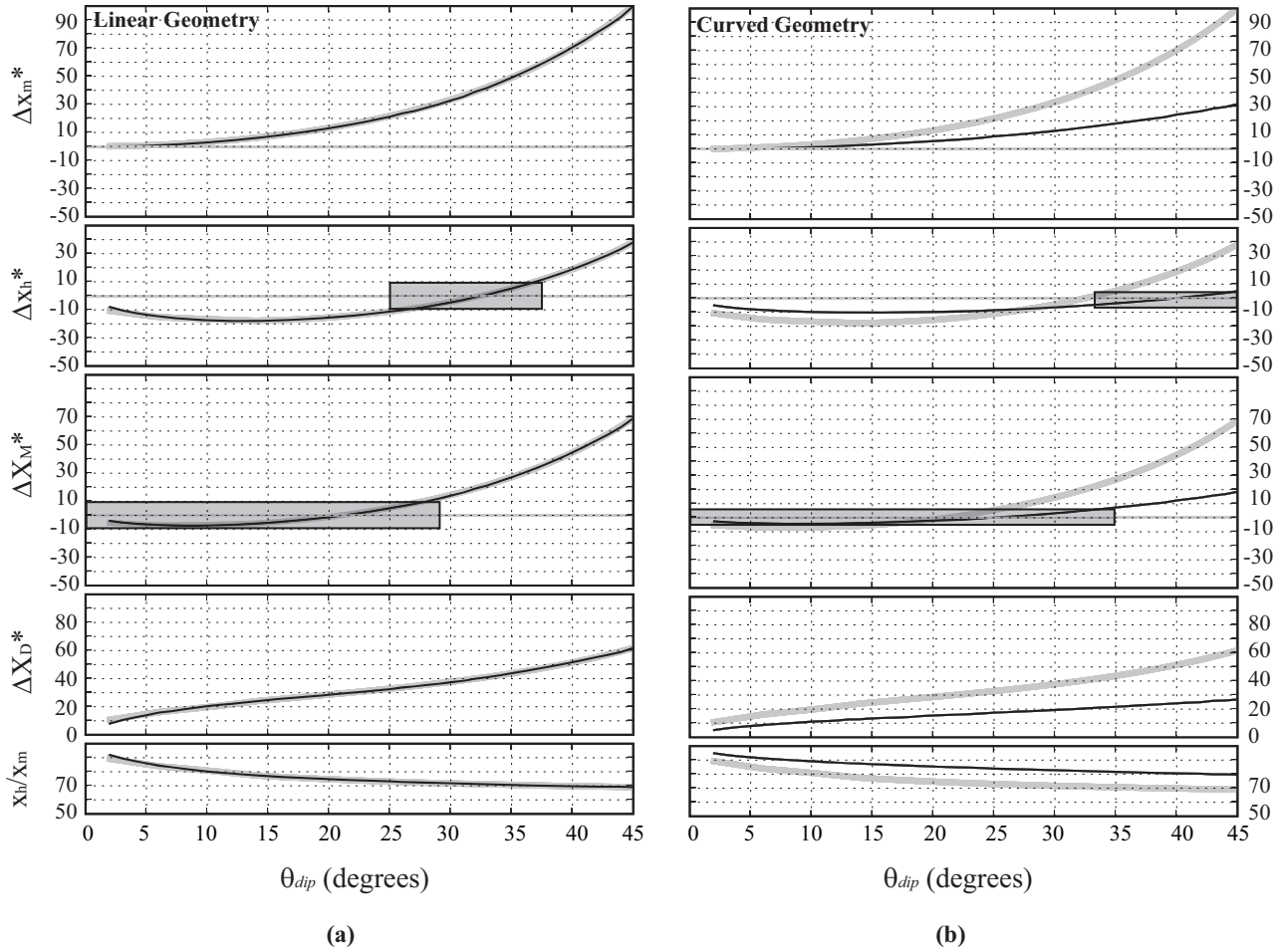
Linear Geometry
Curved Geometry
Δxm*
Δxh*
ΔXM*
ΔXD*
xh/xm
θdip (degrees)
θdip (degrees)
(a)
(b)

Figure 3-6.

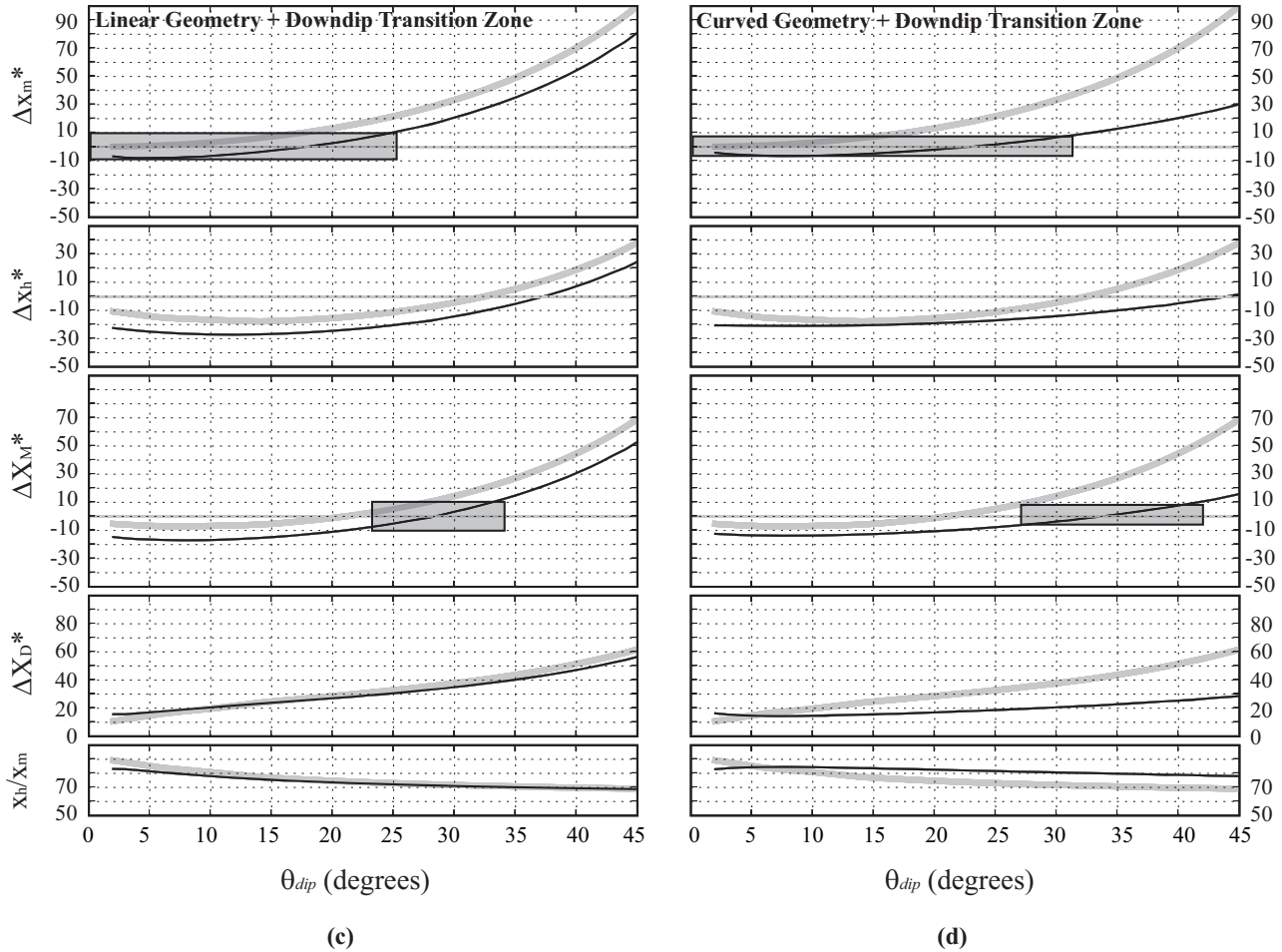

Figure 3-6. Dimensionless plots of the variation in the location of x_{max} and x_{hinge} as a function of fault dip in the BSM having a planar (a, c) or curved (b, d) plate interface geometry, with (c, d) or without (a, b) a transition zone (of fractional length, f_{tr} = 25%) downdip of the locked megathrust zone. See text for definitions of *y*-axis parameters. Top panels: Dimensionless relative distance between x_{max} and x_{lock} (Δx_m*) as a function of the dip of the BSM fault; Second-from-top panels: Dimensionless relative distances between x_{hinge} and x_{lock} (Δx_h*); Third-from-top panels: Mean value of plots in top two panels; Second-from-bottom panel: Difference between the top two panels; Bottom panels: (x_{hinge} /x_{max}). Theoretical estimates for planar faults without any transition zone (thick gray lines from part(a)) are repeated for each panel in parts (b)-(d) for comparison purposes.

Table 3-1 Theoretical Estimates for the horizontal distance between the trench and the surface projection of the downdip end of the locked zone, x_{lock}, for planar and curved faults locked up to the trench. Notation: $\overline{X} = \left(\frac{X_{hinge} + X_{\max}}{2}\right)$, $X_h = X_{hinge}$, $X_m = X_{max}$.

Fault Type	$0° < \theta_{Dip} \leq 25°$	$25° < \theta_{Dip} \leq 35°$	$35° < \theta_{Dip} \leq 45°$
Planar fault	$1.1\,\overline{X} > X_{lock} > 0.9\,\overline{X}$	$1.1\,X_h > X_{lock} > 0.9\,X_h$	$1.0\,X_h > X_{lock} > 0.7\,X_h$
Curved fault (Circular/ Parabolic arc)	$1.05\,\overline{X} > X_{lock} > 0.95\,\overline{X}$	$1.0\,\overline{X} > X_{lock} > 0.9\,\overline{X}$	$1.1\,X_h > X_{lock} > 0.9\,X_h$

Table 3-2. Theoretical Estimates for the horizontal distance between the trench and the surface projection of the bottom of the locked patch, x_{lock}, for planar and curved faults having transition segments immediately downdip of the locked zone. The following results are for transition zones having along-fault lengths of up to 25% of the length of the locked zone. Notation: $\overline{X} = \left(\frac{X_{hinge} + X_{\max}}{2}\right)$, $X_h = X_{hinge}$, $X_m = X_{max}$.

Fault Type	$0° < \theta_{Dip} \leq 25°$	$25° < \theta_{Dip} \leq 35°$	$35° < \theta_{Dip} \leq 45°$
Planar fault	$1.1\,X_m > X_{lock} > 0.9\,X_m$	$1.1\,\overline{X} > X_{lock} > 0.9\,\overline{X}$	$1.0\,X_h > X_{lock} > 0.7\,X_h$
Curved fault (Circular arc)	$1.1\,X_m > X_{lock} > 1.0\,X_m$	$1.0\,X_m > X_{lock} > 0.9\,X_m$	$1.1\,X_h > X_{lock} > 1.0\,X_h$
Curved fault (Parabolic arc)	$1.1\,X_m > X_{lock} > 1.0\,X_m$	$1.1\,\overline{X} > X_{lock} > 0.9\,\overline{X}$	$1.1\,X_h > X_{lock} > 0.9\,X_h$

From the theoretical solutions for planar faults (Figure 3-5(a)), we note that the location of peak vertical uplift rates, X_{max}, changes significantly (by as much as 50% as θ varies from 0° to 45°, as expected from Equation 2. Also, $x_{max} \geq x_{lock}$ always, because comparing (2) and (3), $sec(\theta) \geq cos(\theta)$ (Figure 3-6(a) top and middle). We also plot curves of constant locking depth, D_{lock}, for every 10 km, in the range, 10-50 km (Figure 3-6(a), blue curves). This allows for quantifying x_{max}, x_{hinge}, and x_{lock} for any combination of independent parameters defining the planar BSM (s, θ or D_{lock}). Using the non-dimensionalization discussed above for the dependent variables in Figure 3-5(a), all curves for different fault dimensions, s, collapse into a single curve (Figure 3-6(a)). Dimensional plots for a curved fault are presented in Figure 3-5(b)). In addition to the curves of constant locking depth (blue), another set is included in the upper three panels of this figure for curves of constant radius of curvature, R_p (red), for every 50 km, in the

range, 100–300 km. This allows for quantifying x_{max}, x_{hinge}, and x_{lock} for any combination of independent parameters defining the curved BSM (s, curvature, θ_{bot} or D_{lock}). Theoretical plots for planar faults (yellow curves) are also presented in the bottom two panels of this figure for comparison.

For shallow dips characteristic of most subduction zones ($\theta \leq 30°$ irrespective of geometry, Figure 3-5(a) and (b)), x_{hinge} lies trenchward of x_{lock} (so, Δx_h^* is negative), while x_{max} lies landward of it (Δx_m^* is always positive), but almost equally distant - irrespective of the extent of s_{lock}. We would therefore expect that ΔX_M^* would be a good estimator of x_{lock} for shallow dipping interfaces (third panel of Figure 3-6(a) and (b)) — in fact, this parameter can estimate x_{lock} to within 5 % for planar faults and 2.5 % for curved faults (i.e., with half the uncertainty of using either x_{hinge} or x_{max} alone). To get a feel for the maximum possible difference between these two distances, for s_{lock} ~ 200 km, the difference between x_{hinge} and x_{lock} can vary between 20–40 km for such shallow dipping interfaces. For steeper dips ($30° < \theta \leq 45°$), both x_{hinge} and x_{max} lie on the same side of x_{lock}, with the former being much closer to it (Figure 3-5). So, we would expect x_{hinge} to be a better estimator of x_{lock} compared to x_{max} for steeper plate interfaces (second panel of Figure 3-6(a) and (b)).

In the presence of a transition zone along the plate interface, downdip end of the locked fault — in which slip transitions gradually from zero to the full plate convergence rate — both Δx_h^* and Δx_m^* are negative for dips as high as 40° (Figure 3-6(c) and (d), top). Also, owing to the parameterization of the profile geometries — and given that the effective s_{lock} increases in the presence of a transition zone (Figure 3-1(a) and (b)) — x_{lock} also increases by a factor equal to f_{tz}, irrespective of the fault geometry. Furthermore, x_{max} now becomes much closer to x_{lock} than x_{hinge}. So, in the presence of a downdip transition zone, we would expect x_{max} to be a better estimator of x_{lock} compared to either x_{hinge}, or the mean of x_{hinge} and x_{max} (top panel of Figure 3-6(c) and (d)). However, the uncertainties are almost quadruple the values for faults without any transition zone — that is, x_{max} can be used to estimate x_{lock} to within 20% for planar fault interfaces, and to within 10% for curved interfaces. The ratio x_{hinge}/x_{max} varies between 70 and 90 % for a wide range of

realistic dips of the subduction interface irrespective of both the geometry as well as the presence of a transition zone.

The effect of including the bottom glide surface of the ESPM is to move x_{hinge} trenchward (Figure 2-5; and Kanda and Simons [2010]). For shallow dips ($\theta < 20°$), the effect of bending is small, and the dimensionless parameter curves x_{hinge} are nearly identical to those for the corresponding geometry in Figure 3-6. For steeper dips, x_{hinge} is located trenchward relative to that for the BSM having the same s_{lock} and θ. Therefore, the distance between x_{hinge} and x_{lock} will be negative over a wider range of θ, compared to the corresponding BSM. Also, x_{max} for the ESPM with a finite plate thickness changes little from its value for the ESPM having zero plate thickness (that is, the BSM) [Owen, 2006]. The above results were confirmed for the ESPM having planar or curved interface geometry and different plate thicknesses. In general, we find that x_{lock} for the ESPM can be constrained using the same dimensionless parameter ranges as those for the BSM (Table 3-1 and Table 3-2), for shallow dips (< 20°). Even for the range, $20° < \theta < 30°$, the uncertainty in estimating x_{lock} using these tables is only double that for the corresponding BSM. However, for steeper dips, the uncertainty in estimating x_{lock} from the above surface observables increases significantly.

3.5 Discussion

For megathrust interfaces dipping at an angle of 15° or greater, the distance between x_{hinge} (or x_{max}) and x_{lock} for planar fault geometry is roughly twice that for a curved geometry having the same dip at the downdip end of the locked zone. Also, the location of x_{lock} for a planar fault is much more sensitive to fault dip than for a curved fault (see Figure 3-5, Figure 3-6, and Table 3-1). If geodetic stations are located right above the locked zone (as in Sumatra, for example), then ignoring curvature of the megathrust interface may overpredict vertical uplift rates in that region by as much as 50% (Figure 3-3). Therefore, it is important to constrain fault geometry as tightly as possible before inverting geodetic data. If fault geometry cannot be tightly constrained, then the above uncertainties due to fault geometry should be incorporated into any Bayesian (or Monte-Carlo type) inversion

procedure. Accounting for geometry uncertainties prior to inversion modeling will lead to more realistic families of best-fitting slip-deficit distributions for the megathrust interface. For the ESPM, a tighter *a priori* estimate for interface geometry and s_{lock} also allows better constraints to be placed on the minimum elastic plate thickness [2001].

There is a strong trade-off between including subducting plate thickness and including a transition zone downdip of the locked megathrust (compare Figure 3-1(a) and (b)), especially for horizontal velocities, which have the best signal-to-noise ratio amongst surface velocity components. The horizontal velocity profile for $f_{tr}=0$ for finite plate-thickness (black, Figure 3-1(a), bottom) may be indistinguishable in real life from the $f_{tr}=0.25$ horizontal velocity profile for the BSM (or zero plate thickness case, red in Figure 3-1(b), bottom). This similarity will be more pronounced for subduction zones where plate thickness to locking depth ratio (H/D_{lock}) is 2 or greater (e.g., northeastern Japan, Cascadia, Nicoya Peninsula in Costa-Rica, Peru-Chile trench between Equador and northern Chile, and perhaps Sumatra [see Figure 2-9, and Kanda and Simons, 2010]. As demonstrated with the Monte-Carlo analysis, a similar trade-off exists between the ESPM and a BSM having a wider (and deeper) locked zone (Figure 3-2(c)).

3.6 Conclusions

Here, we quantified the effects of using a more realistic curved plate interface profile, as opposed to a linear fault tangent to it at the downdip end of the locked zone. We note that where the megathrust is not planar, one should still assign backslip onto the actual plate interface (as [1983] originally intended), instead of to a planar fault tangent to the bottom of the locked zone. Irrespective of the fault geometry, we can estimate the surface projection of the downdip end of the locked zone (x_{lock}) from the mean of the locations of x_{hinge} and x_{max}, for most realistic fault dips.

The presence of transition zones broadens the surface velocity profiles landward of the surface projection of the downdip end of the locked zone, and the zone of "broadening" increases with increasing transition zone width. A transition zone can thus smooth the

stresses associated with dislocations while increasing the effective depth of locking. Surface velocities for the curved fault geometry trenchward of x_{max} — the location of the maximum vertical velocities — differ significantly from those due to a planar fault tangent to it at the bottom of the locked zone. However, velocities due to the curved fault landward of x_{max} are nearly identical to those due to the tangent fault. We showed that irrespective of the fault geometry, the mean of x_{hinge} and x_{max} gives a good approximation for x_{lock} for both the BSM and the ESPM with shallow dipping plate interfaces (< 30°). However, in the presence of a transition zone, or a large plate thickness, x_{max} gives a more reliable estimate for x_{lock}, and hence, the extent of the locked zone. Therefore, the common notion that the location of the peak in vertical velocities (x_{max},) determines the extent of the locked megathrust (x_{lock}), is valid only if a transition zone is assumed downdip of the locked interface. Using the BSM instead of the ESPM (having a finite plate thickness, H) for inverting interseismic geodetic data would result in the prediction of a wider (and hence, deeper) locked zone, assuming that the fault geometry is well constrained.

Table 3-3. Notation

θ, θ_{dip}	Planar fault/plate interface dip
θ_{bot}	Dip at the bottom of the locked zone for a curved plate interface
$\Delta\theta$	Change in interface dip from one curved segment to the next
$D_{lock,}$, d_{lock}	Depth of locking along the megathrust interface
d_a	Depth to bottom of updip transition zone, or to the updip limit of locked zone
C_p	Local curvature of the centerline of the plate
f_{tr}	Fractional length of transition zone downdip of locked plate interface, s_{trans}/s_{lock}.
f_a	Fractional depth of updip transition zone w.r.t. locking depth, d_a/d_{lock}.
H	Thickness of the subducting plate in the ESPM
R_p	Local radius of curvature for the centerline of the plate
S	Arc-length along the plate interface, or fault-width
s_{lock}	Width of locked plate interface
s_{trans}	Width of the transition zone downdip of the locked plate interface
Δv	Change in velocity from one plate segment to the next
V_x^*	Horizontal surface velocity normalized by plate rate
V_z^*	Vertical surface velocity normalized by plate rate
ΔX_D^*	Dimensionless distance between x_{max} and x_{hinge}, $(\Delta x_m^* - \Delta x_h^*)$
ΔX_M^*	Mean of dimensionless x_{lock} and x_{max}, $(\Delta x_m^* + \Delta x_h^*)/2$
Δx_h^*	Dimensionless distance between x_{hinge} and x_{lock}, $(x_{hinge} - x_{lock})/x_{lock}$
Δx_m^*	Dimensionless distance between x_{max} and x_{lock}, $(x_{max} - x_{lock})/x_{lock}$
x	Horizontal coordinate, positive landward, or away from the trench
x^*	Horizontal coordinate, normalized w.r.t. locking depth
x_{GPS}	Distance from the trench to the nearest geodetic observation
x_{hinge}	Distance from the trench to the location location of zero vertical surface velocity
x_{lock}	Distance between trench and surface projection of the downdip end of the locked zone
x_{max}	Distance from trench to the location of the peak in the vertical surface velocity field
z	Vertical coordinate, positive upward (depths are therefore, negative)
z^*	Vertical coordinate, normalized w.r.t. locking depth

References

Chlieh, M., J.P. Avouac, K. Sieh, D.H. Natawidjaja and J. Galetzka (2008), Heterogeneous coupling of the Sumatran megathrust constrained by geodetic and paleogeodetic measurements, J. Geophys. Res., 113, B05305, doi:05310.01029/02007JB004981

Chlieh, M., J.B.d. Chabalier, J.C. Ruegg, R. Armijo, R. Dmowska, J. Campos and K.L. Feigl (2004), Crustal deformation and fault slip during the seismic cycle in the North Chile subduction zone, from GPS and InSAR observations, Geophys. J. Int., 158, 695-711.

Cohen, S.C. (1999), Numerical Models of Crustal Deformation in Seismic Zones, Adv. Geophys., 41, 133-231.

Engdahl, E.R., A. Villasenor, H.R. DeShon and C. Thurber (2007), Teleseismic relocation and assessment of seismicity (1918-2005) in the region of the 2004 Mw 9 Sumatra-Andaman and 2005 M 8.7 Nias great earthquakes, Bull. Seismol. Soc. Am., 97 S43-S61.

Freund, L.B. and D.M. Barnett (1976), A Two-Dimensional Analysis of Surface Deformation due to Dip-slip Faulting, Bull. Seismol. Soc. Am., 66, 667-675.

Hsu, Y.-J., M. Simons, J.-P. Avouac, J. Galetzka, K. Sieh, M. Chlieh, D. Natawidjaja, L. Prawirodirdjo and Y. Bock (2006), Frictional Afterslip Following the 2005 Nias-Simeulue Earthquake, Sumatra, Science, 312, 1921-1926.

Hyndman, R.D. and K. Wang (1993), Thermal constraints on the zone of major thrust earthquake failure: The Cascadia subduction zone, J. Geophys. Res., 98, 2039-2060.

Iwasaki, T., W. Kato, T. Moriya, A. Hasemi, N. Umino, T. Okada, K. Miyashita, T. Mizogami, T. Takeda, S. Seikine, T. Matsushima, K. Tashiro and H. Miyamachi (2001), Extensional structure in northern Honshu arc as inferred from seismic refraction/wide-angle reflection profiling, Geophys. Res. Lett., 28, 2329–2332.

Kanda, R.V.S. and M. Simons (2010), An elastic plate model for interseismic deformation in subduction zones, J. Geophys. Res., 115, B03405.

Khazaradze, G. and J. Klotz (2003), Short and long-term effects of GPS measured crustal deformation rates along the South-Central Andes, J. Geophys. Res., 108, 2289.

Masterlark, T. (2003), Finite element model predictions of static deformation from dislocation sources in a subduction zone: Sensitivities to homogeneous, isotropic, Poisson-solid, and half-space assumptions, J. Geophys. Res., 108 2540.

Owen, S.J., 2006. CUBIT 10.2 Documentation, pp. 532, Sandia National Laboratories, Albuquerque, NM, U.S.A.

Rani, S. and S.J. Singh (1992), Static Deformation of a Uniform Half-space due to a Long Dip-slip Fault, Geophys. J. Int., 109, 469-476.

Savage, J.C. (1983), A dislocation model of strain accumulation and release at a subduction zone, J. Geophys. Res., 88 4984-4996.

Savage, J.C. (1995), Interseismic uplift at the Nankai subduction zone, Southwest Japan, 1951–1990, J. Geophys. Res., 100, 6339–6350.

Scholz, C.H. (1990), The Mechanics of Earthquakes and Faulting, edn, vol., pp. 439, Cambridge University Press, New York.

Simoes, M., J.-P. Avouac, R. Cattin and P. Henry (2004), The Sumatra Subduction Zone: A Case for a Locked Fault Zone Extending into the Mantle, J. Geophys. Res., 109, B10402.

Souter, B.J. and B.H. Hager (1997), Fault propagation fold growth during the 1994 Northridge, California, earthquake?, J. Geophys. Res., 102, 11,931–911,942.

Suwa, Y., S. Miura, A. Hasegawa, T. Sato and K. Tachibana (2006), Interplate coupling beneath NE Japan inferred from three-dimensional displacement field, J. Geophys. Res., 111, B04402.

Tomar, S. and N.K. Dhiman (2003), 2-D Deformation Analysis of a Half-space due to a Long Dip-slip Fault at Finite Depth, Proc. Indian Acad. Sci. (Earth Planet. Sci.), 112, 587-596.

Wang, K. and Y. Hu (2006), Accretionary Prisms in Subduction Earthquake Cycles: The Theory of Dynamic Coulomb Wedge, J. Geophys. Res., 111, B06410.

Wang, K., R. Wells, S. Mazzotti, R.D. Hyndman and T. Sagiya (2003), A revised dislocation model of interseismic deformation of the Cascadia subduction zone, J. Geophys. Res., 108, 2026.

Williams, C.A. and R. McCaffrey (2001), Stress rates in the central Cascadia subduction zone inferred from an elastic plate model, Geophys. Res. Lett., 28, 2125-2128.

Zweck, C., J.T. Freymueller and S.C. Cohen (2002), Three-dimensional elastic dislocation modeling of the postseismic response to the 1964 Alaska earthquake, J. Geophys. Res., 107, 2064.